

# Resolving the shock-induced combustion by an adaptive mesh redistribution method

Li Yuan <sup>a,\*</sup>, Tao Tang <sup>b</sup>

<sup>a</sup> *LSEC, Institute of Computational Mathematics, Academy of Mathematics and Systems Science, Chinese Academy of Sciences, Beijing 100080, PR China*

<sup>b</sup> *Department of Mathematics, Hong Kong Baptist University, Kowloon Tong, Hong Kong, PR China*

Received 26 April 2006; received in revised form 5 October 2006; accepted 9 October 2006  
Available online 1 December 2006

---

## Abstract

An adaptive mesh method is presented for numerical simulation of shock-induced combustion. The method is composed of two independent ingredients: a flow solver and a mesh redistribution algorithm. The flow solver is a finite-volume based second-order upwind TVD scheme, together with a lower–upper symmetric Gauss–Seidel relaxation scheme for solving the multispecies Navier–Stokes equations with finite rate chemistry. The adaptive mesh is determined by a grid generation method based on solving Poisson equations, with the monitor function carefully designed to resolve both sharp fronts and the induction zone between them. Numerically it is found that the resolution of the induction zone is particularly critical to the combustion problems, and an under-resolved numerical method may cause excessive energy release and spurious runaway reactions. The monitor function proposed in this paper, which is based on the relative rate of change of mass fraction, covered this issue satisfactorily. Numerical simulations of supersonic flows past an axisymmetric projectile in a premixed hydrogen/oxygen (or air) mixture are carried out. The results show that the spurious runaway chemical reactions appearing on coarse grids can be eliminated by using adaptive meshes without invoking any ad hoc treatment for reaction rates. The adaptive mesh approach is more effective than the fixed mesh one in obtaining grid-independent results. Finally, discrepancies between the numerical and benchmark experimental results and difficulties in simulating the detonation waves are delineated which appeal for further investigation.

© 2006 Elsevier Inc. All rights reserved.

*Keywords:* Adaptive mesh redistribution; Monitor function; Chemically reacting flow; Shock-induced combustion

---

## 1. Introduction

Shock-induced combustion is the self-ignited combustion phenomenon of a premixed gas induced by a shock wave propagating in the gas mixture. There have been extensive experimental and theoretical studies on this phenomenon since 1960s, see, e.g. [1,2]. In the past two decades, it has regained widespread interest

---

\* Corresponding author.

*E-mail addresses:* [lyuan@lsec.cc.ac.cn](mailto:lyuan@lsec.cc.ac.cn) (L. Yuan), [ttang@math.hkbu.edu.hk](mailto:ttang@math.hkbu.edu.hk) (T. Tang).

in aerospace science mainly being a promising combustion mechanism for hypersonic propulsion devices such as pulse detonation engine, oblique detonation wave engine, and ram accelerator [3].

The flowfield of the shock-induced combustion is characterized by the coupling and interactions among the shock wave, combustion front, and combustion instability, which result in various and distinctive flow and wave structures according to the chemical and fluid dynamic conditions. These complicated phenomena pose challenges for numerical simulations. One difficulty is how to capture the coupling and separation between shock and combustion fronts. In reality, when the flight velocity of a projectile in a premixed combustible gas is less than the Chapman–Jouguet (C–J) detonation speed of the gas mixture (referred to as subdetonative speed), the bow shock and the combustion front are separated by a region called induction zone; when the flight velocity is greater than the C–J detonation speed (referred to as superdetonative speed), the bow shock and the combustion front partially merge to form coupled detonative wave structure [1]. The induction zone is a region of nearly constant pressure, temperature and density, yet many reactions with different reaction rates are in progress, giving rise to a release of energy, which may trigger a temperature-sensitive explosion. If the numerical scheme is not accurate enough or the grid size is not sufficiently fine to capture the fastest process, errors in the computed quantities can cause the release of chemical energy much sooner than it should be released due to the extreme temperature sensitivity of reaction rates, resulting in so-called spurious runaway chemical reactions [4]. Standard shock-capturing schemes will lead to nonphysical one-grid-cell per time step spurious detonation velocities when the chemical reactions introduce time scales that are significantly shorter than the flow time scales [5]. Some empirical approaches such as limiting energy release rate or Damköhler number were taken to cure this problem [4,6,7]. However, ad hoc modifications to well defined reaction rates might spoil the underlying physics. Another difficulty that plagues numerical simulations of shock-induced combustion is false combustion instabilities due to the use of inappropriate reaction mechanisms or numerical schemes.

There are numerous studies utilizing adaptive mesh refinement or mesh redistribution methods for providing required spatial resolution in local regions so as to reduce total computational cost (see e.g. [8–14]), but the issue of resolving the induction zone in shock-induced combustion is pervasive in most calculations except few ones where a wavelet adaptive multilevel method [15], or multi-resolution schemes with adaptive grids [16] were used to resolve the induction zone in one-dimensional detonation problems. Recently, the adaptive mesh refinement method was implemented for high-resolution computation of two-dimensional detonation wave structures [17]. The moving mesh method [18] was also utilized to solve the reactive Euler equations and its efficiency was demonstrated for resolving thin structures of the detonation flows. Nevertheless, even if the induction zone was already known crucial in determining the detonation structures [15,19], it was not intentionally resolved in these adaptive mesh simulations.

In this paper, we develop an adaptive mesh redistribution method that is able to resolve shock and combustion waves as well as the induction zone. Adaptive mesh method of this type keeps a simple mesh structure and invariable number of grid points, and has the advantage of separating the mesh redistribution algorithm from the flow solver. For the sake of robustness, we choose a standard second-order upwind total variation diminishing (TVD) scheme of Harten–Yee type [20,21] for the flow solution. The chemical source terms are treated by a pointwise implicit approach instead of splitting approaches, which is in line with the lower–upper symmetric Gauss–Seidel relaxation scheme as implemented in [22]. Once the flow field is updated at a given time level, the grid may be redistributed using an iteration procedure [23,24]. The conventional Poisson grid equation of Thompson et al. [25] is used for mesh redistribution, with its control functions determined from equidistribution of the monitor function along each grid direction in a way similar to [26]. We made slight yet critical modification to the control functions given in [26] for robustness. The peculiarity of the present monitor function is the relative rate of change of mass fractions, which will be shown to be effective for resolving the induction zone. Numerical simulations are compared with Lehr’s experiments [1]. Grid convergence and computational effects for two representative hydrogen/oxygen combustion mechanisms are also demonstrated.

This paper is organized as follows. The governing equations and reaction mechanisms are given in Section 2. The flow solution method is listed in Section 3, and the adaptive mesh redistribution algorithm is described in Section 4. Numerical simulations of the steady-state flows corresponding to flow conditions in Lehr’s experiments are given in Section 5 and discrepancies between simulations and experiments are delineated. Conclusions are presented in Section 6.

## 2. Governing equations

The governing equations for the chemically reacting viscous flows are the compressible Navier–Stokes equations with chemical source terms for a mixture composed of  $N$  gas species, which are expressed in the following form:

$$\frac{\partial \mathbf{Q}}{\partial t} + \frac{\partial \mathbf{E}}{\partial x} + \frac{\partial \mathbf{F}}{\partial y} = \frac{\partial \mathbf{E}_v}{\partial x} + \frac{\partial \mathbf{F}_v}{\partial y} + \mathbf{H} + \mathbf{H}_v + \mathbf{S}, \quad (1)$$

where

$$\mathbf{Q} = [\rho_1, \dots, \rho_N, \rho u, \rho v, \rho E]^T, \quad (2)$$

$$\mathbf{E} = [\rho_1 u, \dots, \rho_N u, \rho u^2 + p, \rho uv, u(\rho E + p)]^T, \quad (3)$$

$$\mathbf{F} = [\rho_1 v, \dots, \rho_N v, \rho uv, \rho v^2 + p, v(\rho E + p)]^T, \quad (4)$$

$$\mathbf{E}_v = [\rho D_1 \frac{\partial c_1}{\partial x}, \dots, \rho D_N \frac{\partial c_N}{\partial x}, \tau_{xx}, \tau_{xy}, u\tau_{xx} + v\tau_{xy} + q_x]^T, \quad (5)$$

$$\mathbf{F}_v = \left[ \rho D_1 \frac{\partial c_1}{\partial y}, \dots, \rho D_N \frac{\partial c_N}{\partial y}, \tau_{xy}, \tau_{yy}, u\tau_{xy} + v\tau_{yy} + q_y \right]^T, \quad (6)$$

$$\mathbf{H} = -\frac{m}{y} [\rho_1 v, \dots, \rho_N v, \rho uv, \rho v^2, v(\rho E + p)]^T, \quad (7)$$

$$\mathbf{H}_v = \frac{m}{y} \left[ \rho D_1 \frac{\partial c_1}{\partial y}, \dots, \rho D_N \frac{\partial c_N}{\partial y}, \tau_{xy}, \tau_{yy} - \tau_{\theta\theta}, u\tau_{xy} + v\tau_{yy} + q_y \right]^T, \quad (8)$$

$$\mathbf{S} = (\dot{\omega}_1, \dots, \dot{\omega}_N, 0, 0, 0)^T \quad (9)$$

and

$$\tau_{xx} = 2\mu \frac{\partial u}{\partial x} - \frac{2}{3} \mu \nabla \cdot \mathbf{u} = \frac{2}{3} \mu \left( 2 \frac{\partial u}{\partial x} - \frac{\partial v}{\partial y} - \frac{mv}{y} \right), \quad (10)$$

$$\tau_{yy} = 2\mu \frac{\partial v}{\partial y} - \frac{2}{3} \mu \nabla \cdot \mathbf{u} = \frac{2}{3} \mu \left( 2 \frac{\partial v}{\partial y} - \frac{\partial u}{\partial x} - \frac{mv}{y} \right), \quad (11)$$

$$\tau_{xy} = \mu \left( \frac{\partial u}{\partial y} + \frac{\partial v}{\partial x} \right), \quad (12)$$

$$\tau_{\theta\theta} = 2\mu \frac{v}{y} - \frac{2}{3} \mu \nabla \cdot \mathbf{u}, \quad (13)$$

$$q_x = \lambda \frac{\partial T}{\partial x} + \rho \sum_{k=1}^N D_k h_k \frac{\partial c_k}{\partial x}, \quad (14)$$

$$q_y = \lambda \frac{\partial T}{\partial y} + \rho \sum_{k=1}^N D_k h_k \frac{\partial c_k}{\partial y}. \quad (15)$$

The equations describe two-dimensional plane flow if  $m = 0$  and axisymmetric flow if  $m = 1$ .  $u$  and  $v$  are velocity components,  $p$  is the pressure,  $T$  is the temperature,  $E$  is the total energy per unit mass,  $\rho_k$  is the density of species  $k$ , with total density  $\rho = \sum_{k=1}^N \rho_k$ ,  $c_k = \rho_k / \rho$  is the mass fraction,  $\dot{\omega}_k$  is the mass production rate of species  $k$  due to chemical reactions,  $h_k$  is the specific enthalpy,  $D_k$  is the mass diffusivity of species  $k$  in the mixture defined as

$$D_k = (1 - X_k) \left/ \sum_{j \neq k} \frac{X_j}{D_{kj}} \right.,$$

where  $D_{kj}$  is the binary diffusivity,  $X_k$  is the mole fraction, and  $\mu$  and  $\lambda$  are dynamic viscosity and thermal conductivity of the gas mixture, respectively. The diffusive transport coefficients,  $\mu$  and  $\lambda$ , are determined using

Wilke's semi-empirical formula with  $\mu_k$  and  $\lambda_k$  of each species found from NASA thermodynamic data [27]. For high speed flow simulations, mass diffusion is greatly simplified by neglecting pressure diffusion and thermal diffusion, and assuming the binary diffusivity  $D_{kj}$  to be equal between all components [28]. Its value is obtained by assuming a constant Schmidt number  $S_c = \mu/(\rho D_{kj}) = 0.5$ , see [27].

It is assumed that all species are thermally perfect, in thermal equilibrium and have the same temperature. The equation of state is that for a mixture of thermally perfect gases

$$p = \sum_{k=1}^N \frac{\rho_k}{M_k} R_u T, \quad (16)$$

where  $M_k$  is the molecular weight of species  $k$  and  $R_u$  is the universal gas constant. The total energy per unit volume  $\rho E$  is used for implicit evaluation of temperature  $T$  by the Newton iteration method through the thermodynamic relationship  $\rho e = \rho h - p$ , i.e.

$$\rho E - \frac{1}{2} \rho \mathbf{u}^2 = \sum_{k=1}^N \rho_k \left( \int_{T_0}^T \frac{C_{p_k}}{M_k} dT' + h_k^0 \right) - R_u T \sum_{k=1}^N \frac{\rho_k}{M_k}, \quad (17)$$

where  $C_{p_k}$  is the specific heat at constant pressure, and  $h_k^0$  is the heat of formation at reference temperature  $T_0$ . The specific heats are expressed as functions of temperature in polynomial fit

$$\frac{C_{p_k}}{R_u} = a_{1k} + a_{2k}T + a_{3k}T^2 + a_{4k}T^3 + a_{5k}T^4, \quad (18)$$

where the coefficients  $a_{ik}$  can be obtained from thermodynamic data file of the chemical kinetics package (CHEMKIN [29]) or from NASA thermochemical polynomial data [30], which are often valid in certain temperature ranges. The appropriate speed of sound for the thermally perfect gas mixture model is the frozen speed of sound

$$a^2 = \sum_{k=1}^N c_k p_{\rho_k} + (\gamma - 1)(H - \mathbf{u}^2)$$

with  $H = h + \frac{1}{2} \mathbf{u}^2$ ,  $p_{\rho_k} = (\gamma - 1)(\frac{1}{2} \mathbf{u}^2 - h_k) + \gamma R_u T / M_k$ , and  $\gamma = C_p / (C_p - R)$ , where  $\gamma$  can be calculated from the frozen specific heat  $C_p = \sum_{k=1}^N c_k C_{p_k}$  and mixture gas constant  $R = R_u \sum_{k=1}^N c_k / M_k$ .

In realistic combustion, the general formula for a reaction mechanism with  $I$  elementary reactions is expressed as

$$\sum_{k=1}^N v'_{ki} X_k \rightleftharpoons \sum_{k=1}^N v''_{ki} X_k, \quad i = 1, \dots, I. \quad (19)$$

The mass production rate for each species is

$$\dot{\omega}_k = M_k \sum_{i=1}^I (v''_{ki} - v'_{ki}) \left[ k_{f_i} \prod_{k=1}^N \left( \frac{\rho_k}{M_k} \right)^{v'_{ki}} - k_{b_i} \prod_{k=1}^N \left( \frac{\rho_k}{M_k} \right)^{v''_{ki}} \right], \quad k = 1, \dots, N. \quad (20)$$

where the forward and backward reaction rate constants for the  $i$ th reaction,  $k_{f_i}$  and  $k_{b_i}$ , are given in Arrhenius formula (omitting the subscripts f, b for clarity)

$$k_i = A_i T^{B_i} \exp(-C_i/T). \quad (21)$$

Two reaction mechanisms for H<sub>2</sub>-air mixture combustion are used and their simulation effects will be compared. One is Evans and Schxnayder's 12-species 25-step reaction scheme [31], another is Jachimowski's 13-species 33-step reaction scheme [32]. The first 16 and 19 reactions in Refs. [31,32], respectively, are used for H<sub>2</sub>/O<sub>2</sub> mixture combustion.

### 3. Flow solution method

The governing equations for chemically reacting flows are often stiff. There are usually two kinds of approach to solve stiff systems: the splitting approach which decouples fluid dynamics from chemical kinetics, and the non-splitting one which solves the fully coupled equations simultaneously. In the present study we use the latter approach as implemented in [22]. The governing equations (1) are integrated over a quadrilateral mesh cell

$$\int_{\Omega} \frac{\partial \mathbf{Q}}{\partial t} d\Omega + \oint_{\partial\Omega} (\mathbf{f} \cdot \mathbf{n}) dS = \int_{\Omega} (\mathbf{H} + \mathbf{H}_v + \mathbf{S}) d\Omega, \tag{22}$$

where  $\mathbf{f} = (\mathbf{E} - \mathbf{E}_v)\mathbf{i} + (\mathbf{F} - \mathbf{F}_v)\mathbf{j}$ . By virtue of divergence theorem, we can obtain the semi-discretized finite volume formulation for a rectangular mesh cell

$$\left( \Omega \frac{\partial \mathbf{Q}}{\partial t} \right)_{I,J} + (\hat{\mathbf{E}}_{i+1} - \hat{\mathbf{E}}_i)_J + (\hat{\mathbf{F}}_{j+1} - \hat{\mathbf{F}}_j)_I = (\hat{\mathbf{E}}_{v,i+1} - \hat{\mathbf{E}}_{v,i})_J + (\hat{\mathbf{F}}_{v,j+1} - \hat{\mathbf{F}}_{v,j})_I + [\Omega(\mathbf{H} + \mathbf{H}_v + \mathbf{S})]_{I,J}, \tag{23}$$

where uppercase  $I, J$  denote the center of a mesh volume  $\Omega$ , and lowercase  $i, j$  denote the cell faces,  $\hat{\mathbf{E}}_i = (\mathbf{E}\mathbf{i} + \mathbf{F}\mathbf{j}) \cdot (\mathbf{nS})_i$ ,  $\hat{\mathbf{E}}_{v,i} = (\mathbf{E}_v\mathbf{i} + \mathbf{F}_v\mathbf{j}) \cdot (\mathbf{nS})_i$ . By applying backward time difference, linearization of all flux derivative terms and chemical source terms at  $n + 1$  time level with respect to  $n$  level, and first-order upwind scheme for resulting terms containing inviscid flux Jacobians, we obtain the fully discretized incremental form:

$$\left( \frac{\Omega}{\Delta t} \mathbf{I} - \Omega \mathbf{P} + \mathbf{A}^+ - \mathbf{A}^- + \mathbf{B}^+ - \mathbf{B}^- + \mathbf{A}_i^v + \mathbf{A}_{i+1}^v + \mathbf{B}_j^v + \mathbf{B}_{j+1}^v \right)_{I,J} \times \Delta \mathbf{Q}_{I,J} - (\mathbf{A}_{I-1}^+ + \mathbf{A}_{i,I-1}^v) \Delta \mathbf{Q}_{I-1,J} + (\mathbf{A}_{I+1}^- + \mathbf{A}_{i+1,I+1}^v) \Delta \mathbf{Q}_{I+1,J} - (\mathbf{B}_{J-1}^+ + \mathbf{B}_{j,J-1}^v) \Delta \mathbf{Q}_{I,J-1} + (\mathbf{B}_{J+1}^- + \mathbf{B}_{j+1,J+1}^v) \Delta \mathbf{Q}_{I,J+1} = \text{RHS}^n, \tag{24}$$

where

$$\text{RHS}^n = -(\hat{\mathbf{E}}_{i+1} - \hat{\mathbf{E}}_i)_J^n - (\hat{\mathbf{F}}_{j+1} - \hat{\mathbf{F}}_j)_I^n + (\hat{\mathbf{E}}_{v,i+1} - \hat{\mathbf{E}}_{v,i})_J^n + (\hat{\mathbf{F}}_{v,j+1} - \hat{\mathbf{F}}_{v,j})_I^n + \Omega(\mathbf{H} + \mathbf{H}_v + \mathbf{S})^n, \tag{25}$$

$\Delta \mathbf{Q} = \mathbf{Q}^{n+1} - \mathbf{Q}^n$ ,  $\mathbf{P} = \partial \mathbf{S} / \partial \mathbf{Q}$  is the Jacobian matrix of chemical source vector which is  $N \times N$  in size as simplified in [22],  $\mathbf{A}^{\pm}$  and  $\mathbf{B}^{\pm}$  are split Jacobian matrices of inviscid fluxes, where we have used the approximate flux Jacobian splitting  $\mathbf{A}^{\pm} = \frac{1}{2}(\mathbf{A} \pm \lambda_A \mathbf{I})$ , with  $\mathbf{A} = \partial \hat{\mathbf{E}} / \partial \mathbf{Q}$  being the inviscid flux Jacobian and  $\lambda_A$  its maximum absolute eigenvalue. The viscous Jacobian matrices are

$$\begin{aligned} \mathbf{A}_{i,I-1}^v &= -\partial \hat{\mathbf{E}}_{v,i} / \partial \mathbf{Q}_{I-1}, & \mathbf{A}_{i,I}^v &= \partial \hat{\mathbf{E}}_{v,i} / \partial \mathbf{Q}_I, \\ \mathbf{A}_{i+1,I}^v &= -\partial \hat{\mathbf{E}}_{v,i+1} / \partial \mathbf{Q}_I, & \mathbf{A}_{i+1,I+1}^v &= \partial \hat{\mathbf{E}}_{v,i+1} / \partial \mathbf{Q}_{I+1}. \end{aligned} \tag{26}$$

Eq. (24) is iteratively solved by the LU-SGS scheme

$$\lambda D_{I,J}^* - (\mathbf{A}_{I-1}^+ + \mathbf{A}_{i,I-1}^v) D_{I-1,J}^* - (\mathbf{B}_{J-1}^+ + \mathbf{B}_{j,J-1}^v) D_{I,J-1}^* = \text{RHS}^n, \tag{27a}$$

$$\lambda \Delta \mathbf{Q}_{I,J} + (\mathbf{A}_{I+1}^- + \mathbf{A}_{i+1,I+1}^v) \Delta \mathbf{Q}_{I+1,J} + (\mathbf{B}_{J+1}^- + \mathbf{B}_{j+1,J+1}^v) \Delta \mathbf{Q}_{I,J+1} = \lambda D_{I,J}^*, \tag{27b}$$

where

$$\lambda = \left( \frac{\Omega}{\Delta t} \mathbf{I} - \Omega \mathbf{P} + \mathbf{A}^+ - \mathbf{A}^- + \mathbf{B}^+ - \mathbf{B}^- + \mathbf{A}_i^v + \mathbf{A}_{i+1}^v + \mathbf{B}_j^v + \mathbf{B}_{j+1}^v \right)_{I,J}.$$

In the evaluation of  $\text{RHS}^n$ , the diffusive terms are approximated by the conventional central difference [33], and the inviscid numerical flux vector are approximated by the second-order upwind TVD scheme due to Harten–Yee [20,21]

$$\tilde{\hat{\mathbf{E}}}_{i+1} = \frac{1}{2} [\hat{\mathbf{E}}_{i+1}(\mathbf{Q}_I) + \hat{\mathbf{E}}_{i+1}(\mathbf{Q}_{I+1}) + \mathbf{R}_{i+1} \Phi_{i+1}], \tag{28}$$

where  $\mathbf{R}_{i+1}$  is a matrix whose column vectors are the right eigenvectors of  $\mathbf{A}$  evaluated at some symmetric average of  $\mathbf{Q}_I$  and  $\mathbf{Q}_{i+1}$ , denoted as  $\mathbf{Q}_{i+1}$  [34]. The element  $\phi_{i+1}^I$  of the dissipation vector  $\Phi_{i+1}$  for Harten–Yee scheme is

$$\phi_{i+1}^I = \sigma(\lambda_{i+1}^I)(g_I^I + g_{I+1}^I) - \psi(\lambda_{i+1}^I + \gamma_{i+1}^I)\alpha_{i+1}^I, \tag{29}$$

where  $\lambda_{i+1}^I$  is the eigenvalue of  $\mathbf{A}$  evaluated at  $\mathbf{Q}_{i+1}$ ,  $\alpha_{i+1}^I$  is the element of the vector  $\alpha_{i+1} = \mathbf{R}_{i+1}^{-1}(\mathbf{Q}_{I+1} - \mathbf{Q}_I)$ , and  $g_{i+1}^I$  is the limiter function. The function  $\sigma(z)$  and variable  $\gamma_{i+1}^I$  are

$$\sigma(z) = \frac{1}{2} \left[ \psi(z) - \frac{\Delta t}{\Omega} z^2 \right], \tag{30}$$

$$\gamma_{i+1}^I = \sigma(\lambda_{i+1}^I) \begin{cases} (g_{i+1}^I - g_I^I)/\alpha_{i+1}^I, & \alpha_{i+1}^I \neq 0, \\ 0, & \alpha_{i+1}^I = 0. \end{cases} \tag{31}$$

The entropy function is given by

$$\psi(z) = \begin{cases} |z|, & |z| \geq \epsilon, \\ \frac{z^2 + \epsilon^2}{2\epsilon}, & |z| < \epsilon, \end{cases} \tag{32}$$

where  $\epsilon$  is an empirical coefficient. The limiter function used is

$$g_I^I = \frac{\alpha_i^I(\alpha_{i+1}^I)^2 + \alpha_{i+1}^I(\alpha_i^I)^2}{(\alpha_i^I)^2 + (\alpha_{i+1}^I)^2}. \tag{33}$$

#### 4. Adaptive mesh redistribution

The present adaptive mesh redistribution method follows from an earlier one by Tang and Tang [23], which is of grid-location type and has the advantage of decoupling the mesh redistribution from the flow evolution. A continuous conservative interpolation procedure is used for transferring flow variables from previous to next grid in the iteration process. However, it did not allow grid anisotropy. To achieve grid anisotropy, we use the conventional Poisson grid generation equation due to Thompson et al. [25] to generate and redistribute a structured quadrilateral mesh

$$\begin{aligned} \nabla^2 \xi &= \frac{g_{22}}{g} P, \\ \nabla^2 \eta &= \frac{g_{11}}{g} Q, \end{aligned} \tag{34}$$

where  $g_{11} = x_\xi^2 + y_\xi^2$ ,  $g_{22} = x_\eta^2 + y_\eta^2$ , and  $P$  and  $Q$  are called control functions which determine the grid point distribution. For finite difference solution, the above system is inverted into the computational domain by interchanging its dependent and independent variables so as to solve for  $x, y$  on the computational domain:

$$g_{22}(\mathbf{r}_{\xi\xi} + P\mathbf{r}_\xi) + g_{11}(\mathbf{r}_{\eta\eta} + Q\mathbf{r}_\eta) - 2g_{12}\mathbf{r}_{\xi\eta} = 0, \tag{35}$$

where  $\mathbf{r} = (x, y)$ ,  $g_{12} = \mathbf{r}_\xi \cdot \mathbf{r}_\eta$ . The determination of  $P$  and  $Q$  depends on whether they are for initial grid generation or for grid redistribution. In the first case when the initial grid is to be generated, the distribution of grid points on the boundary is given. From the boundary grid points, the control functions  $P$  along  $\xi$ -line boundaries, and  $Q$  along  $\eta$ -line boundaries are determined from projection analysis

$$\begin{aligned} P &= -\frac{\mathbf{r}_\xi \cdot \mathbf{r}_{\xi\xi}}{|\mathbf{r}_\xi|^2}, \\ Q &= -\frac{\mathbf{r}_\eta \cdot \mathbf{r}_{\eta\eta}}{|\mathbf{r}_\eta|^2}, \end{aligned} \tag{36}$$

and are further modified to take into account the orthogonality on boundaries and the curvature effect [25]. The interior  $P(\xi, \eta)$  and  $Q(\xi, \eta)$  are subsequently obtained through one-directional interpolation in the

computational domain. We denote the initial control functions as  $P_0$  and  $Q_0$ , which will play an anchoring role in subsequent grid adaptation.

In the second case when the grid is to be redistributed, the control functions  $P$  and  $Q$  are in principle obtained from so-called monitor functions  $\omega_1$  and  $\omega_2$  in  $\xi$  and  $\eta$  curvilinear coordinate direction, respectively. The monitor functions indicate solution errors in some sense [35]. It is very important to choose an appropriate monitor function, otherwise the adaptive effect cannot be realized no matter how good a moving mesh algorithm is. Several strategies for designing monitor functions have been proposed e.g. [36,37]. According to Anderson’s analysis [26], the equidistribution of the monitor function  $\omega_i$  along a coordinate line  $\xi_i$  is equivalent to setting control functions as

$$\begin{aligned} P &= \frac{1}{\omega_1} \frac{\partial \omega_1}{\partial \xi}, \\ Q &= \frac{1}{\omega_2} \frac{\partial \omega_2}{\partial \eta}. \end{aligned} \tag{37}$$

However, we have found that using (37) alone would lead to severely twisted grids near the body surface, resulting in breakdown of a viscous flow computation. To increase robustness, we let  $(P, Q)$  be weighted averages between (37) and initial ones

$$(P, Q)^T = \alpha(P, Q)^T + (1 - \alpha)(P_0, Q_0)^T, \tag{38}$$

where  $\alpha = (\min(j, j_c) - 1)/(j_c - 1)$ , and  $j_c$  is a prescribed index in the direction normal to the wall corresponding roughly to the outer edge of the boundary layer. The grid generation system (35) is solved using Gauss–Seidel iteration. After each iteration, the flow variables  $\mathbf{Q}$  are transferred from the previous grid  $G^p$  to the next grid  $G^{p+1}$  by a monotonic conservative interpolation procedure [23]. This enables calculation of the monitor functions, hence the control functions for the next iteration. The boundary grid points are also redistributed according to the tangential displacement of the neighboring interior grid points when necessary. In order to maintain a smooth mesh for the viscous flow computation, boundary grid points on the body surface are not redistributed.

To achieve grid adaptation near shock and combustion fronts, the following monitor function is often used

$$\omega_i = \sqrt{1 + \beta_1 \left( \frac{\partial \bar{T}}{\partial \xi_i} \right)^2}, \tag{39}$$

with  $\bar{T}$  being the non-dimensional temperature, and  $\beta_1$  the adaptivity constant, see e.g. [37–39]. However, an efficient monitor function within the induction zone is not obvious due to essentially constant density, pressure and temperature in this region. It is believed that many reactions are occurring, giving rise to variation in compositions of some chemical species. We have observed large gradients in logarithmic scale of the mass fractions of some radical species just before the combustion front. The variation of logarithmic mass fraction is equivalent to the relative rate of change of mass fraction, namely,

$$\frac{\partial \ln \bar{c}_k}{\partial \xi_i} = \frac{1}{\bar{c}_k} \frac{\partial \bar{c}_k}{\partial \xi_i}, \tag{40}$$

where  $\bar{c}_k = \max(c_k, 10^{-9})$  is the tailored mass fraction. Therefore, we suggest a monitor function

$$\omega_i = \sqrt{1 + \beta_1 \left( \frac{\partial \bar{T}}{\partial \xi_i} \right)^2 + \beta_2 \left[ \max_k \left( \left| \frac{1}{\bar{c}_k} \frac{\partial \bar{c}_k}{\partial \xi_i} \right| \right) \right]^2}, \tag{41}$$

where  $\beta_1$  and  $\beta_2$  are adaptivity constants. The term  $\frac{1}{\bar{c}_k} \frac{\partial \bar{c}_k}{\partial \xi_i}$  can capture large variations of  $\bar{c}_k$  even if the magnitude of  $\bar{c}_k$  is small in the induction zone. In the induction zone  $\bar{c}_k$  itself may be very small in magnitude, but its variation is critical. Thus, using a relative rate of change makes better sense than using rate of change directly. Indeed, the monitor function (41) is found to give adequate adaption both in the induction zone and near the shock and combustion fronts.

A summary of the adaptive mesh redistribution algorithm is given below:

- (1) Generate the initial grid using the elliptic grid generation system (35), with  $P_0, Q_0$  obtained from given boundary grid point distributions and interpolations.
- (2) Advance the flow solution  $M$  steps by the LU-SGS scheme (27a).
- (3) In the next time step, after the  $M$  steps with the LU-SGS scheme, do grid redistribution:
  - (a) Calculate the monitor function  $\omega_i$  from (41) and do 1–2 times spatial smoothing on  $\omega_i$ , then calculate the control functions  $P, Q$  by the weighted averaging (38).
  - (b) Solve Eq. (35) by one iteration of Gauss–Seidel relaxation to get new grid  $G^{p+1}$ .
  - (c) Interpolate the flow solution  $\mathbf{Q}$  from old grid  $G^p$  onto the new grid  $G^{p+1}$  by using the conservative interpolate procedure given in [23].
  - (d) The iteration procedure (a)–(c) on grid redistribution and flow solution interpolation is continued until the grid do not change significantly from one iteration to the next.
- (4) Start new time step (go to step 2).

## 5. Numerical examples and discussions

Two test cases of shock-induced combustion corresponding to Figs. 1 and 5 in Lehr's benchmark experiments [1] were selected to testify the present adaptive method. A spherical projectile with a diameter of 15 mm is flying at supersonic speeds 1892 m/s ( $M = 3.55$ ) and 2605 m/s ( $M = 6.46$ ) in a stoichiometric  $\text{H}_2/\text{O}_2$  ( $2\text{H}_2 + \text{O}_2$ ) and  $\text{H}_2/\text{air}$  ( $2\text{H}_2 + \text{O}_2 + 3.76\text{N}_2$ ) mixture of temperature 293 K at pressure of 186 and 320 mmHg, respectively. Since the detonation speeds of the two mixtures are 2550 and 2055 m/s, respectively, then  $M = 3.55$  corresponds to the subdetonative speed and  $M = 6.46$  corresponds to the superdetonative speed. We will use  $M = 3.55$  case to demonstrate the effect of mesh adaptation on elimination of spurious runaway chemical reactions, and the effect of the new monitor function, and use  $M = 6.46$  case to compare detonation structures. The computational domain may include either a hemisphere or a hemisphere plus a cylinder of one diameter in length. Non-slip, adiabatic, and non-catalytic boundary conditions are used on the body surface. All the computations are initialized from the free-stream conditions and are assumed to reach steady state when the residual drops to  $10^{-5}$ .

### 5.1. Role of adaptive mesh and the monitor function

Fig. 1 shows the fixed and adaptive grids and corresponding temperature contours for  $M = 3.55$  case. It can be seen from Fig. 1b that both the shock wave and the combustion front go out of the computational domain for the fixed grid computation. The result implies spurious runaway chemical reactions because they are contrary to experimental stationary shock and combustion fronts. This artifact occurs on low-resolution  $65^2$  grid but not on  $129^2$  and finer grids. However, adaptive mesh calculations using traditional monitor function (39) or present one (41) show that the shock and combustion fronts are captured inside the computational domain on  $65^2$  grid, and temperature contours for both monitors are virtually identical as shown in Fig. 1d. Furthermore, we can see from Fig. 1e that the adaptive mesh obtained with the new monitor function (41) is clustered not only near the shock and combustion fronts, but also in the induction zone between them.

We discuss the spurious runaway chemical reactions as shown in Fig. 1b a bit further. They are related to excessive release of chemical energy in one grid cell in a single time step in numerical calculation of shock-deflagration problems [4]. If the time step chosen according to the CFL condition is not small enough to resolve chemical reactions, or inexact discretization or insufficient spatial resolution appears near the deflagration, then numerical errors will falsely trigger a temperature-sensitive chemical reaction earlier than it should be. We have found that a low-order numerical scheme is more prone to produce spurious runaway reactions than a high-order one, and that chemical kinetics used also has influence on runaway reactions. For example, calculation with Jachimowski' mechanism produce runaway reactions on  $33^2$  but not on  $65^2$  grids. In general situations when a reaction mechanism contains very fast exothermic reactions, remedies such as limiting the

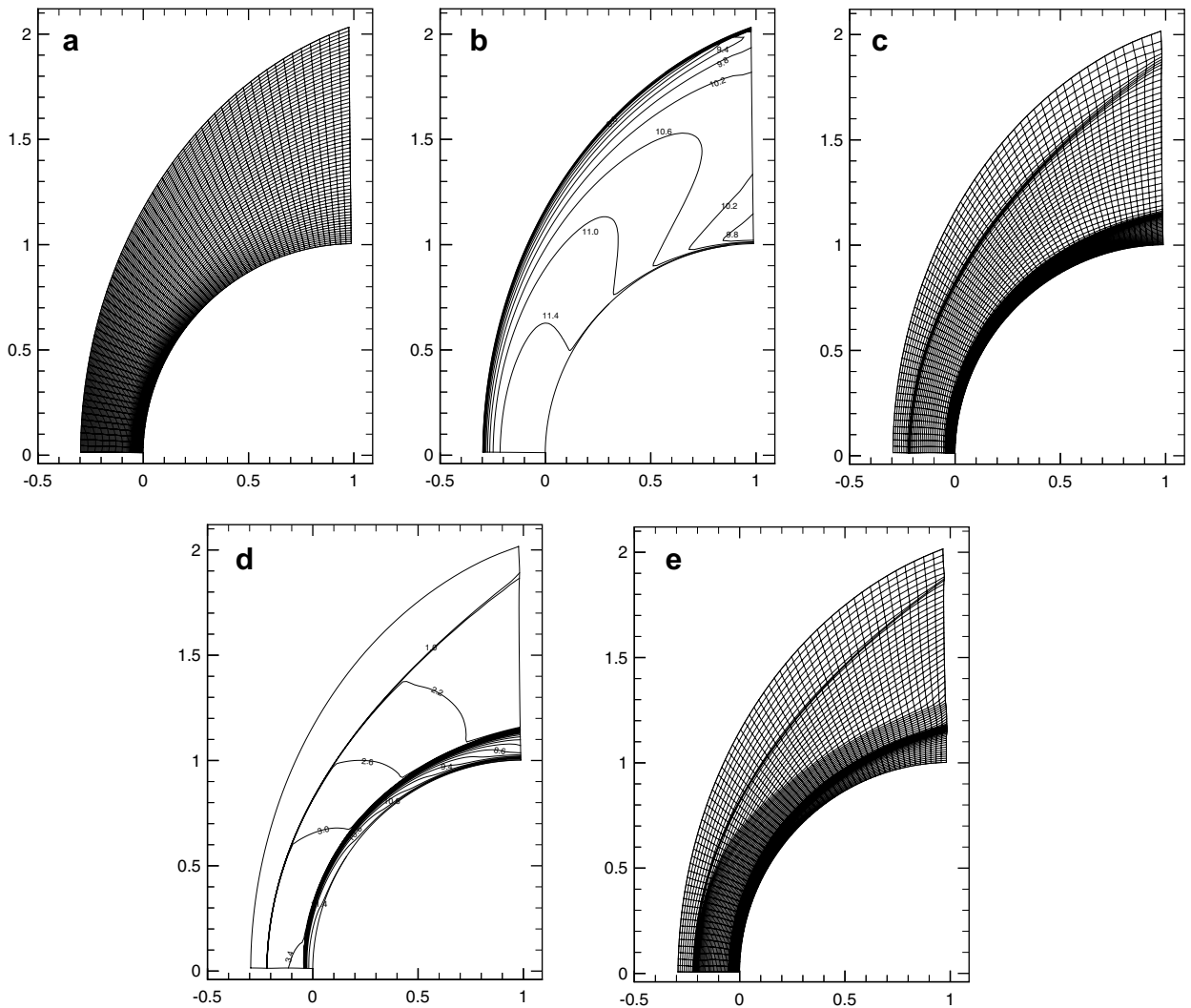


Fig. 1. Fixed (a) and adaptive grids (c,e), and corresponding temperature contours for  $T/T_\infty$  (b,d) computed using  $65^2$  grid points for  $M = 3.55$  flow in stoichiometric  $H_2/O_2$  mixture. (c) and (d) are obtained using the conventional monitor function (39), and (e) shows the adaptive grid using the present monitor function (41). Evans' reaction mechanism [31] is used throughout.

energy release rate or Damköhler number [4,6,7], or adopting infinitely fast chemistry model, have to be invoked. However, ad hoc limiting to reaction rates should be avoided. We see the adaptive mesh computation is an alternative approach for eliminating spurious runaway reactions with fewer grid points because it can provide sufficient spatial resolution near deflagration fronts.

## 5.2. Grid convergence tests

Fig. 2 shows temperature distributions along the front stagnation line for  $M = 3.55$  case calculated by using successively fine grid points. One can see that the distributions converge on  $195^2$  adaptive grids, but they do not even on  $385^2$  fixed grids. It seems that the adaptive mesh calculation on  $129^2$  grid at least can give well converged shock location. If the results on  $195^2$  adaptive grids are thought to be equivalent to those on  $385^2$  fixed grids, it roughly translates into half CPU time saving for the adaptive mesh calculation.

We remark that the converged position of the shock and deflagration fronts are also different for different reaction mechanisms. The shock and deflagration fronts obtained with Evans' mechanism are further away

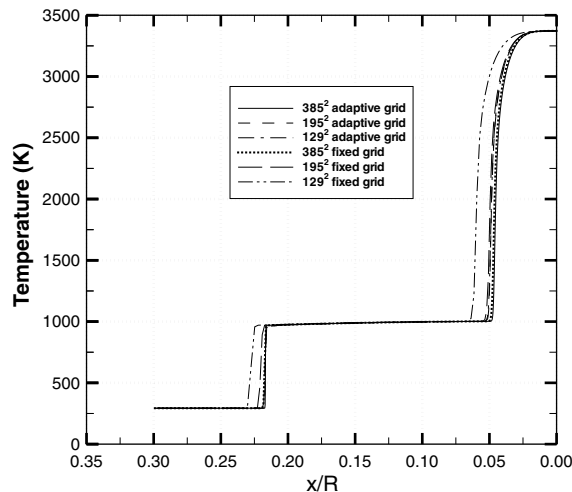


Fig. 2. Temperature along the stagnation streamline for adaptive and fixed grids using three successively fine grid points.  $M = 3.55$  flow. Evans' reaction mechanism is used throughout.

from the body and in better agreement with the experiment. However, Evans' mechanism is prone to cause numerical unsteady combustion on heavily adapted grids in contrast to the steady state combustion observed in the experiment for  $M = 6.46$  hydrogen/air case, while Jachimowski's mechanism is not so easy. In this regard, Jachimowski's mechanism is more robust than Evans'. We will go back to discuss this issue in the next subsection.

Fig. 3 shows comparison between the calculated density contours and the experimental shadowgraph image for  $M = 3.55$  case. The computational domain extends one sphere diameter to the cylindrical portion where supersonic outflow boundary conditions are used on the exit plane. We see fair agreement between the calculation and the experiment in the upstream, however, the computation does not predict the more inclined combustion front and the second shock wave originating from the deflected combustion front in the flank of the afterbody as appeared in the experiment. This discrepancy may be attributed to inaccurate modeling of viscous effects, ignorance of the flow transition and base flow region, or other unknown reasons. Further investigation may include base flow region and turbulence modeling, which is not perused in this paper.

### 5.3. $M = 6.46$ hydrogen/air case

The  $M = 6.46$  case corresponds to the superdetonative speed, where the shock wave and the deflagration front are coupled near the front stagnation line and separated as soon as the velocity component normal to the bow shock wave is equal to the detonation velocity [1]. The exact position of the separation is very sensitive to the amount of heat release, hence depends on the reaction mechanism used. Several numerical studies have tested the appropriateness of different reaction mechanisms using this case (see [40] and references therein). However, these earlier calculations used relatively smaller number of grid points that doomed to predict a smaller induction zone than in the experiment, and in particular, veil potential numerical combustion instability due to excessive numerical diffusions present on coarse grids. Based on the grid convergence test in Section 5.2, we compare the computational effects between Evan's and Jachimowski's mechanisms using more than  $195^2$  grid points.

Figs. 4a–f compare the density contours for a hemisphere domain calculated with both reaction mechanisms on fixed and adaptive grids, respectively. It is seen that the combustion front computed with Evans' mechanism separates from the shock wave earlier and the induction zone is larger than computed with Jachimowski's mechanism, which indicates the former mechanism is better in matching numerical results with the experimental one. One can also see that the density contours on  $195^2$  adaptive grid (Figs. 4c and d) are comparable to or better than those on  $385^2$  fixed grid (Figs. 4a and b). The adaptive  $385^2$  grid (Fig. 4e) provides little improvement over  $195^2$  adaptive grid because the adaptive extent is limited by numerical combustion

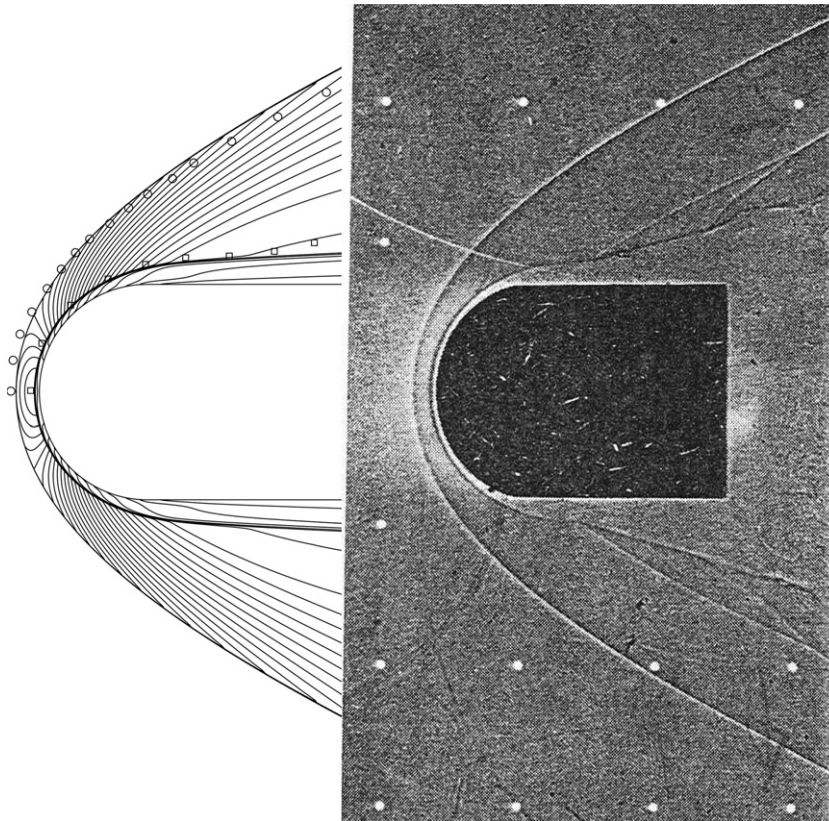


Fig. 3. Comparison of calculated density contours with experimentally obtained shock position (○), combustion front (□) and shadowgraph [1] for  $M = 3.55$   $\text{H}_2/\text{O}_2$  flow. The adaptive mesh has  $513^2$  grid points. Evans' reaction mechanism is used.

instabilities occurring on highly adaptive grids for Evans' mechanism. Nevertheless, it provides evident improvement for Jachimowski's mechanism as the mesh adaptivity enhances the solution resolution without causing combustion instabilities (Fig. 4f).

Figs. 5a and b show comparisons of calculated density contours in the domain with the cylindrical afterbody on  $513^2$  adaptive grids. We can see the shock and combustion fronts for two mechanisms are comparable to the experimental positions. However, the calculated induction zone is smaller in the upstream and wider in the downstream than in the experiment. Again, the induction zone computed with Evans' mechanism is larger than with Jachimowski's mechanism, showing the former is in better agreement with the experiment in the upstream region.

At this point, we discuss difficulties encountered in the numerical computations of this particular case. In obtaining the adaptive grid results, we found that each grid redistribution must be followed by a long, fixed-grid computation to obtain nearly convergent flowfield; otherwise, consecutive adaptive computation would lead to unrealistic, extensive combustion instabilities which subsequently result in dramatic grid redistributions to make computation not convergent to steady state. In our computation, only 1–2 times mesh adaptations are allowed, further adaptations would again cause unrealistic combustion instabilities.

To find out whether the nonsmoothness of adaptive meshes or the fine mesh size itself is responsible for numerical combustion instability, calculations were conducted on  $769^2$  and  $1025^2$  fixed grid. We found both mechanisms can converge to steady state on  $769^2$  grid and predicted qualitatively the same result as the experimental, but there are unrealistic combustion instabilities on  $1025^2$  grid. To our relief, calculations on  $1025^2$  grid can converge to steady state for a chemically frozen flow. It is thus believed that the numerical combustion instability is caused by very fine mesh size. Thus, the case of  $M = 6.46$  presents a particular difficulty associated with numerical simulation of detonation waves by using detailed chemistry: when a high resolution mesh is desirable for eliminating runaway reactions, an excessive fine mesh might lead to false unstable

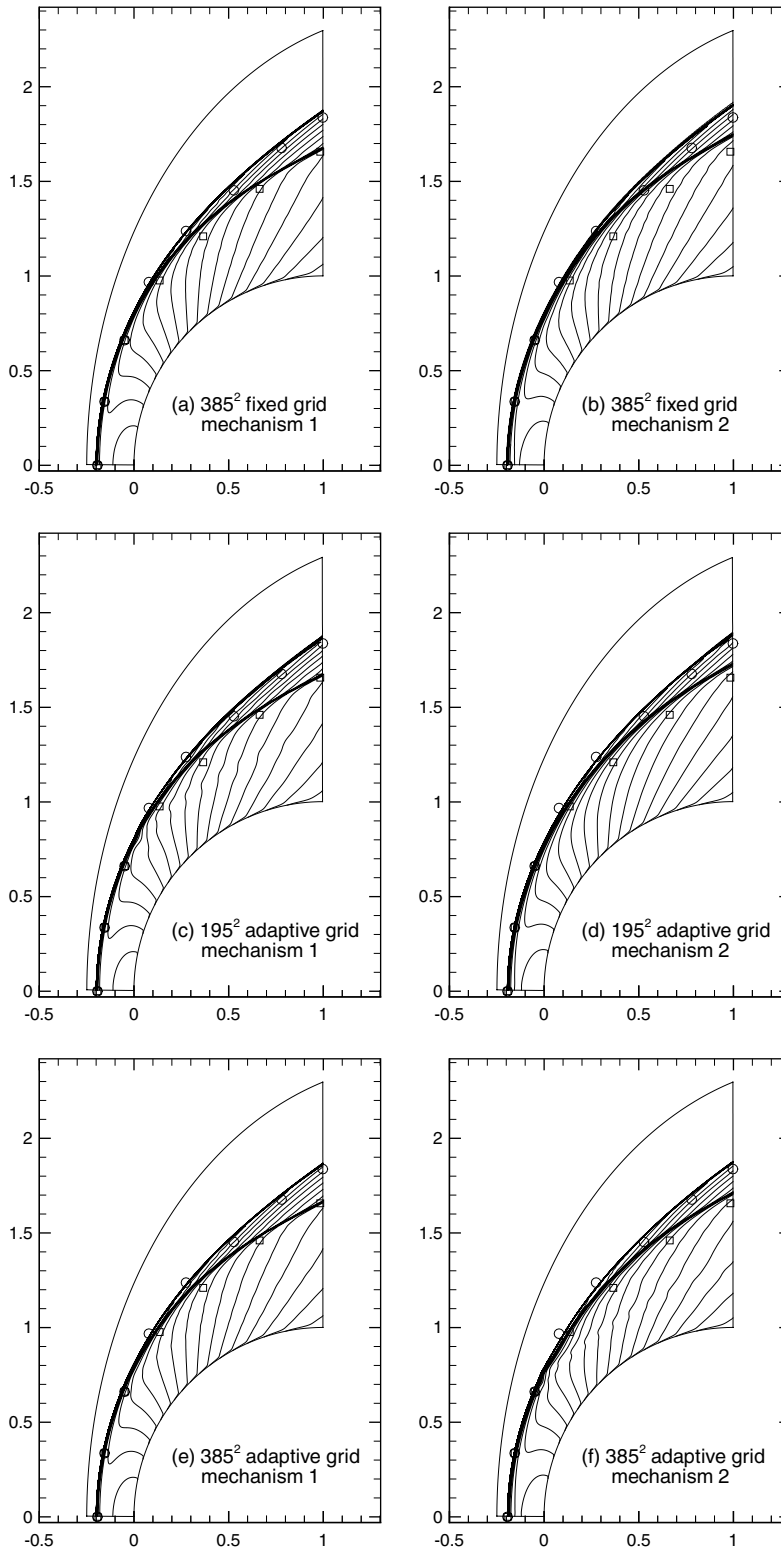


Fig. 4. Comparison of calculated density contours and experimental obtained shock position (○) and combustion front (□) for  $H_2/Air$  and  $M = 6.46$  flow between Evans' reaction mechanism [31] (left column) and Jachimowski's mechanism [32] (right column) on 385<sup>2</sup> fixed, 195<sup>2</sup> adaptive, and 385<sup>2</sup> adaptive grids, respectively.

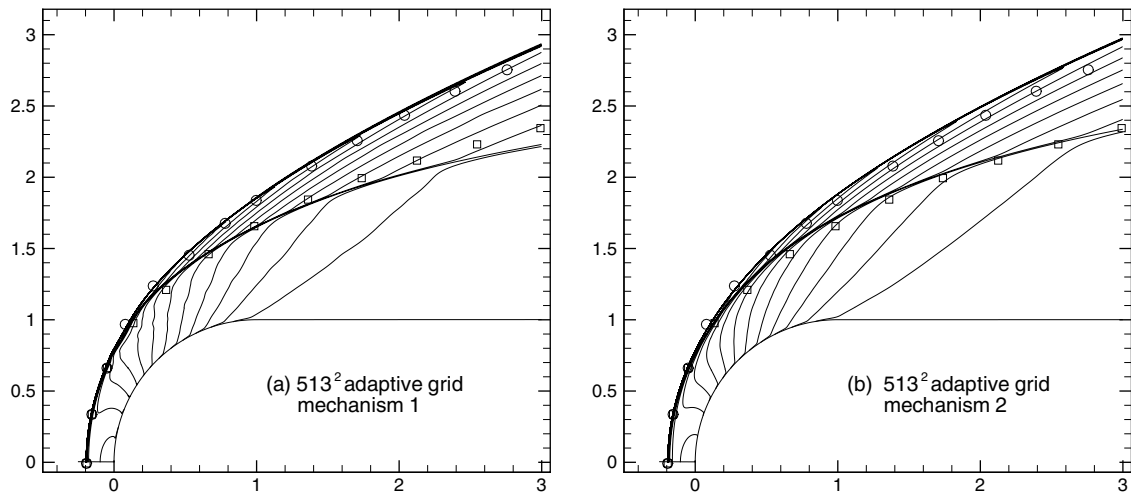


Fig. 5. Comparisons of calculated density contours obtained with (a) reaction mechanism 1 [31] and (b) mechanism 2 [32] on  $513^2$  adaptive grid for  $H_2/air$   $M = 6.46$  flow. The experimental shock is marked with (○) and the combustion front with (□).

combustion. We are not sure if it is caused by some subtle interactions of chemical reactions with numerical errors. The efficiency of an adaptive mesh method will then be limited by such interactions. We present this dilemma to call for others' attention.

## 6. Conclusions

We have developed an adaptive mesh redistribution method for numerical simulation of shock-induced combustion. We demonstrate the efficiency of the adaptive method in eliminating spurious runaway chemical reactions and obtaining grid-independent results. One of the main contributors to the high resolution of the adaptive grid method is the monitor function (41) which is based on the relative rate of change of  $c_k$ 's. The choice of the monitor function is found extremely important for the shock-induced combustion problems due to large ratios of many variables involved. The proposed monitor function (41) can resolve the induction zone between the shock wave and combustion front. Our numerical results on moderately fine grids are in fair agreement with classic experiments. Nevertheless, simulations of  $M = 3.55$  case do not reproduce experimentally observed deflection of the combustion front and the secondary shock in the flank of the projectile. Furthermore, false combustion instabilities occur with very fine mesh or consecutive mesh adaptation for  $M = 6.46$  case. These two unsolved problems appeal for further investigation.

## Acknowledgments

We thank the referee for pointing out the equivalence relationship (40) which gives a useful explanation for the monitor function (41). This work was supported by Natural Science Foundation of China (G10476032, G10531080), state key program for developing basic sciences (2005CB321703), CERG Grants of Hong Kong Research Grant Council and FRG Grants of Hong Kong Baptist University. The computation was conducted on Origin 3800 SMP computer at LSEC of Institute of Computational Mathematics, Chinese Academy of Sciences.

## References

- [1] H.F. Lehr, Experiments on shock-induced combustion, *Astron. Acta* 17 (1972) 589–597.
- [2] J.B. McVey, T.Y. Toong, Mechanism of instabilities of exothermic hypersonic blunt-body flow, *Combust. Sci. Technol.* 3 (1971) 63–79.
- [3] J.E. Shepherd, Detonation waves and propulsion, in: J. Buckmaster, T. Jackson, A. Kumar (Eds.), *Combustion in High-speed Flows*, Kluwer, Dordrecht, The Netherlands, 1994, pp. 373–420.
- [4] E.S. Oran, J.P. Boris, *Numerical Simulation of Reactive Flow*, Elsevier, New York, 1987 (Chapter 13).

- [5] P. Colella, A. Majda, V. Roytburd, Theoretical and numerical structure for reacting shock waves, *SIAM J. Sci. Comput.* 7 (1986) 1059–1080.
- [6] S. Yungster, S. Eberhardt, A. Bruckner, Numerical simulation of hypervelocity projectiles in detonable gases, *AIAA J.* 29 (1991) 187–199.
- [7] V.N. Gamezo, E.S. Oran, Reaction-zone structure of a steady-state detonation wave in a cylindrical charge, *Combust. Flame* 109 (1997) 253–265.
- [8] G. Beckett, J.A. Mackenzie, M.L. Robertson, An  $r$ -adaptive finite element method for the solution of the two-dimensional phase-field equations, *Commun. Comput. Phys* 1 (2006) 805–826.
- [9] M.J. Berger, R.J. LeVeque, Adaptive mesh refinement using wave-propagation algorithms for hyperbolic systems, *SIAM J. Numer. Anal.* 35 (1998) 2298–2316.
- [10] Y. Di, P. Zhang, Moving mesh kinetic simulation for sheared rodlike polymers with high potential intensities, *Commun. Comput. Phys.* 1 (2006) 859–873.
- [11] R. Li, T. Tang, P.-W. Zhang, Moving mesh methods in multiple dimensions based on harmonic maps, *J. Comput. Phys.* 170 (2001) 562–588.
- [12] F. Losasso, R. Fedkiw, S. Osher, Spatially adaptive techniques for level set methods and incompressible flow, *Comput. Fluids* 35 (2006) 995–1010.
- [13] P.A. Zegeling, On resistive MHD models with adaptive moving meshes, *J. Sci. Comput.* 24 (2005) 263–284.
- [14] X. Zeng, J. Lowengrub, A. Anderson, V. Cristini, Adaptive unstructured volume remeshing – II: application to two- and three-dimensional level-set simulations of multiphase flow, *J. Comput. Phys.* 208 (2005) 626–650.
- [15] S. Singh, Y. Rastigejev, S. Paolucci, J. Powers, Viscous detonation in  $H_2$ – $O_2$ –Ar using intrinsic low-dimensional manifolds and wavelet adaptive multilevel representation, *Combust. Theory Modelling* 5 (2001) 163–184.
- [16] B. Bihari, D. Schwendeman, Multiresolution schemes for the reactive Euler equations, *J. Comput. Phys.* 154 (1999) 197–230.
- [17] R. Deiterding, Parallel adaptive simulation of multi-dimensional detonation structures, Ph.D. Thesis, Techn. U. Cottbus, September, 2003.
- [18] B. Azarenok, T. Tang, Second-order Godunov scheme for reactive flow calculations on moving meshes, *J. Comput. Phys.* 206 (2005) 48–80.
- [19] A. Matsuo, K. Fujii, Flow features of shock-induced combustion around projectile travelling at hypervelocities, *AIAA J.* 33 (1995) 1056–1063.
- [20] A. Harten, High resolution schemes for hyperbolic conservation laws, *J. Comput. Phys.* 49 (1983) 357–393.
- [21] H.C. Yee, A class of high-resolution explicit and implicit shock-capturing methods, NASA TM 101088, 1989 (unpublished).
- [22] J. Shuen, S. Yoon, Numerical study of chemically reacting flows using a lower–upper symmetric successive overrelaxation scheme, *AIAA J.* 27 (1989) 1752–1760.
- [23] H.Z. Tang, T. Tang, Adaptive mesh methods for one- and two-dimensional hyperbolic conservation laws, *SIAM J. Numer. Anal.* 41 (2003) 487–515.
- [24] H.Z. Tang, T. Tang, P.-W. Zhang, An adaptive mesh redistribution method for nonlinear Hamilton–Jacobi equations in two- and three dimensions, *J. Comput. Phys.* 188 (2003) 543–572.
- [25] J.F. Thompson, Z.U.A. Warsi, C.W. Mastin, *Numerical Grid Generation: Foundations and Applications*, North-Holland, Amsterdam, 1985, Chapter IV. Available from <http://www.erc.msstate.edu/publications/gridbook/chap06/index.html>.
- [26] D.A. Anderson, Equidistribution schemes, Poisson generators, and adaptive grids, *Appl. Math. Comput.* 24 (1987) 211–227.
- [27] R.N. Gupta, J.M. Yos, R.A. Thompson, A review of reaction rates and thermodynamic and transport properties for the 11-species air model for chemical and thermal nonequilibrium calculations to 30000K, NASA TM 101528, 1989.
- [28] T. Poinso, D. Veynante, *Theoretical and Numerical Combustion*, R.T. Edwards, Inc., 2001.
- [29] R.J. Kee, F.M. Rupley, E. Meeks, J.A. Miller, Chemkin-III: a Fortran chemical kinetics package for the analysis of gas-phase chemical and plasma kinetics, UC405, SAND 96-8216, 1996.
- [30] W.C. Gardiner Jr., *Combustion Chemistry*, Springer, New York, 1984.
- [31] J.S. Evans, C.J. Schexnayder, Influence of chemical kinetics and unmixedness on burning in supersonic hydrogen flames, *AIAA J.* 18 (1980) 188–193.
- [32] C.J. Jachimowski, An analytic study of the hydrogen-air reaction mechanism with application to scramjet combustion, NASA TP-2791, February, 1988.
- [33] F.A. Greene, R.U. Gupta, Viscous equilibrium computations using LAURA, *J. Spacecraft Rockets* 29 (5) (1992) 627–632.
- [34] M. Vinokur, Flux Jacobian matrices and generalized Roe average for an equilibrium real gas, NASA CR-177512, 1988.
- [35] V.D. Liseikin, *Grid Generation Methods*, Springer, Berlin, 1999 (Chapter 7).
- [36] W.M. Cao, W.Z. Huang, R.D. Russell, An error indicator monitor function for an  $r$ -adaptive finite-element method, *J. Comput. Phys.* 170 (2001) 871–892.
- [37] H.-Z. Tang, A moving mesh method for the Euler flow calculations using a directional monitor function, *Commun. Comput. Phys.* 1 (2006) 656–676.
- [38] W.M. Cao, W.Z. Huang, R.D. Russell, An  $r$ -adaptive finite element method based upon moving mesh *PDEs*, *J. Comput. Phys.* 149 (1999) 221–244.
- [39] R. Li, T. Tang, P.W. Zhang, A moving mesh finite element algorithm for singular problems in two and three space dimensions, *J. Comput. Phys.* 177 (2002) 365–393.
- [40] K. Clutter, V. Krishnamurty, W. Shyy, Combustion and turbulent effects in hypersonic projectile flows, AIAA Paper 97-0807, 1997.